

Analysis of the osteogenic and mechanical characteristics of iron ($\text{Fe}^{2+}/\text{Fe}^{3+}$)-doped β -calcium pyrophosphate

Emaan Alsubhe^{a,*}, Antonios D. Anastasiou^b, Mozhdeh Mehrabi^a, El Mostafa Raif^c,
Ali Hassanpour^a, Peter Giannoudis^d, Animesh Jha^{a,*}

^a School of Chemical and Process Engineering, University of Leeds, LS2 9JT Leeds, UK

^b Department of Chemical Engineering and Analytical Science, University of Manchester, UK

^c Division of Oral Biology, School of Dentistry, University of Leeds, UK

^d Leeds Institute of Rheumatic and Musculoskeletal Medicine, University of Leeds, UK

ARTICLE INFO

Keywords:

Brushite
 β -calcium pyrophosphate
Iron phosphate
Mechanical properties
Osteogenic cells

ABSTRACT

The calcium phosphate is the main mineral constituent of bone. Although there has been significant amount of research on finding ideal synthetic bone, no suitable scaffold material has yet been found. In this investigation, the iron doped brushite ($\text{CaHPO}_4 \cdot 2\text{H}_2\text{O}$) has been investigated for osteogenic potential and mechanical properties. The synthesis of iron-oxide doping in the form of $\text{Fe}^{2+},^{3+}$ -ions were carried out using the solution based method in which the ammonium hydrogen phosphate and calcium nitrate solutions were used in stoichiometric ratio for synthesizing $\text{CaHPO}_4 \cdot 2\text{H}_2\text{O}$, with doping concentrations of $\text{Fe}^{2+},^{3+}$ -ions between 5 mol% and 30 mol%. The synthesized powders were analysed using X-ray powder diffraction, FTIR, SEM and Raman spectroscopic techniques. The heat treatment of synthesized powder was carried out at 1000 °C in air for 5 h, and it was found that the dominant crystalline phase in samples with < 20 mol% was β -CPP, which also formed an iron-rich solid solution phase. Increasing the concentrations of $\text{Fe}^{2+},^{3+}$ -ions enhances the phase fraction of FePO_4 and amorphous phase. Amongst the $\text{Fe}^{2+},^{3+}$ -doped β -CPP minerals, it was found that the 10 mol% $\text{Fe}^{2+},^{3+}$ -doped β -CPP offers the best combination of bio-mechanical and osteogenic properties as a scaffold for bone tissue regenerative engineering.

1. Introduction

Bone is a multiphase tissue, in which hydroxyapatite (HAP) ($\text{Ca}_5(\text{PO}_4)_3(\text{OH})$) is the dominant inorganic phase, with collagen, blood vessels and bone marrow [1,2] to be the soft material. The hard HAP mineral is combined with collagen fibers to form the strong, lightweight structure that supports the body weight and ambulation. By comparison, blood vessels and bone marrow provide a physiological environment for maintaining continuous tissue regeneration and biological function. Due to this elaborate structure the healing of bone is a complex physiological process and certain conditions should be satisfied for a successful result. Giannoudis and co-authors reported [3] that the following four factors must be present in order to achieve the restoration of damaged and fractured bone: a) osteogenic and osteo-conducting environment for cells to grow and colonise the scaffold, b) angiogenesis, c) growth factors for controlling and stimulating bone growth, and d) bio-mechanical stabilization for promoting healing with implanted grafts. These four factors are known as the “Diamond

Concept” and underpin the standard approach for achieving healing and bone remodelling. Based on the above defined underpinning factors for bone tissue restoration, the most important materials challenge is the development of biomaterials and scaffolds that present both enhanced osteogenic potential and also appropriate the mechanical properties to provide required mechanical stability. By adopting this approach, the enhancement in vascularity and growth factors may be achieved using the technique of harvesting platelet rich plasma during surgery [4], after a damaged area is stabilised with an osteogenic and bio-mechanically strong implant. A mechanically unstable bone leads to compromised healing and non-union [5], demanding further surgical intervention and risk of procrastinated healing [6] due to other comorbid factors [7].

Calcium phosphate (CaP) minerals, which include HAP, are well known for their structural similarities with the natural mineral of bone and thus have been investigated extensively for a broad range of applications related to the restoration of hard tissues. Although the minerals are well known for many decades, in a recent review paper by

* Corresponding authors.

E-mail addresses: ml13eha@leeds.ac.uk (E. Alsubhe), a.jha@leeds.ac.uk (A. Jha).

<https://doi.org/10.1016/j.msec.2020.111053>

Received 28 February 2020; Received in revised form 20 April 2020; Accepted 3 May 2020

Available online 08 May 2020

0928-4931/© 2020 The Authors. Published by Elsevier B.V. This is an open access article under the CC BY license (<http://creativecommons.org/licenses/by/4.0/>).

Habraken et al., [8] the CaPs are characterised as the “biomaterials of the future” since they are easily certifiable, they have low synthesis cost, they present extraordinary biological performance (e.g. are non-toxic, biocompatible and promote mineralisation) and also their properties can be tailored through cationic and/or anionic substitutions. The disadvantage of CaP, especially those with OH-bonds, namely, HAp, brushite (also known as DCPD ($\text{CaHPO}_4 \cdot 2\text{H}_2\text{O}$)) and monetite (CaHPO_4) are intrinsically brittle and therefore, unable to support load after fracture stabilization of long bone defects. Historically, several different types of doping ions (e.g. Mg^{2+} , Sr^{2+} , Zn^{2+}) have been investigated as substitutional cations in the calcium phosphate minerals for improving the biocompatible and cell supporting properties. The primary reason for studying iron substitution is to analyze in the role of such minerals in bone environment where the redox reaction may be controlled via the two oxidation (2+, 3+) states of iron. Since the bone mineral carries load, the importance of load carrying mechanical properties (e.g. hardness) are essential together with the biological (cell supporting) properties of the minerals. In recent works, it has been demonstrated that doping calcium phosphates with iron oxide improves dramatically the mechanical properties of the minerals, particularly after sintering [9,10]. For example, Anastasiou et al. [9], reported that the hardness of 10 mol% iron doped β -pyrophosphate [β -CPP: (β - $\text{Ca}_2\text{P}_2\text{O}_7$)] after sintering reached to 265 HK value while, the hardness of the undoped material under identical sintering conditions is nearly 8 times lower (32.5 HK). Besides the beneficial effect on mechanical properties of CaP, doping with iron found also to improve the osteogenic potential of the minerals. Manchon et al. [11], investigated the in vivo behaviour of Fe^{2+} , Fe^{3+} -doped β -tricalcium phosphate, showing proliferation of osteoblasts and osteocytes leading to formation of new bone with a network of vasculature after 8 weeks of implantation. Similar results have been also reported by Panseri et al. [12], who introduced Fe^{2+} and Fe^{3+} ions into hydroxyapatite structure to synthesise superparamagnetic nanoparticles. Even without static magnetic field, the iron containing NPs demonstrated excellent biocompatibility and increased proliferation of human osteoblast-like cells comparing to commercial HaP NPs.

Although there are numerous published works that discuss the doping of calcium phosphate minerals with iron oxide at different concentrations [13–16]. It is however unclear which is the most suitable doping concentration for promoting osteogenesis in a bio-mechanically stable environment. The main goal in this article is to characterise the effect of iron oxide doping concentration on the structure, phase combination, mechanical properties, biocompatibility and regenerative potential of iron doped calcium phosphate minerals.

From the phase transformation studies, it is evident that the calcium pyrophosphate is one of the intermediate phases that forms during resorption before bone mineralisation occurs in vivo [17]. Also, during in vitro experiments, it was demonstrated that the pyrophosphate triggers enzymatic action which accelerates the resorption of the phosphate mineral. The evidence for β -CPP mineral resorption via enzymatic action dispels previous hypothesis that the mineral phase inhibits bone remineralisation [18]. Unlike other calcium phosphates minerals, for example HAp and brushite, the β -CPP is least understood mineral for bone scaffold engineering, which is why in this investigation different concentrations of iron ion (0, 5, 10, 20 and 30 mol%) have been analysed for the synthesis of β -CPP, and studied in more detail using X-Ray powder diffraction (XRPD), scanning electron microscopy (SEM), Fourier-transform infrared spectroscopy (FTIR) and nano-indentation techniques. The iron ions doped and undoped β -CPP were also analysed for osteogenic potential using a range of cell-based tests, discussed below, for quantifying the regenerative potential of the scaffold.

2. Materials and methods

2.1. Preparation of minerals

The β -CPP mineral phase was obtained after heat treatment of DCPD [19]. For the precursor synthesis, 200 mL of a 0.1 M Ca (NO_3) $_2 \cdot 4\text{H}_2\text{O}$ (Fisher Chemicals, CAS:13477-34-4) aqueous solution (solution A), was heated to 37 °C. At this temperature, 0.1 M (NH_4) $_3\text{PO}_4$ (Acros Organics, CAS:7783-28-0) solution (200 mL) was added dropwise to solution A. The mixture was continuously stirred at 37 °C for 2 h, and then left to settle for 1 h for allowing the precipitation of DCPD ($\text{CaHPO}_4 \cdot 2\text{H}_2\text{O}$) Chemical formula). The precipitated crystals were collected on a filter paper (Whatman grade 44 with pores of 3 μm), washed several times with distilled water and then dried for 24 h at 80 °C. For the synthesis of the iron oxide doped brushite (Fe-DCPD), a similar procedure, as described above for solution A, was followed however before mixing with the (NH_4) $_3\text{PO}_4$ solution, the required dopant concentrations of iron nitrate powder ($\text{Fe}(\text{NO}_3)_3 \cdot 9\text{H}_2\text{O}$ (0, 5, 10, 20, 30 mol%) (VWR Chemicals, CAS:7782-61-8) was incorporated into solution A. During the synthesis, it was observed that the addition of the iron nitrate resulted in a significant pH change from pH 5.5 for DCPD to 2.1 for the 30Fe-DCPD. However, when attempts were made to buffer the solution at pH = 5.5, it promoted the formation of formation of undesirable iron oxide nanoparticles.

The undoped and iron oxide doped powders were heat treated at 1000 °C in air for 5 h, which was empirically found to be sufficient for the transformation of brushite into β -pyrophosphate (Table 1).

For testing the mechanical properties of the materials and for cell growth experiments, the powders of DCPD and doped DCPD were pressed into pellets using a 13 mm diameter die. For each pellet approximately 0.25 g of the DCPD powder was filled into the cylindrical cavity of the die before pressing with a load of 6 ton for 15 min. After pressing, the pellets were heat treated to 1000 °C for 5 h in air and then cooled down to room temperature.

2.2. Characterisation methodologies

The phase constitution of the synthesized DCPD powder and sintered crystalline materials was analysed using a Philips X'Pert MPD X-Ray powder diffractometer equipped with a monochromatic Cu K α radiation source ($\lambda = 1.54 \text{ \AA}$). Each analyte was scanned for Bragg angles (2θ) between 10° and 60° with an angular step of 0.065° and a traverse speed of 0.014132° s $^{-1}$. For the analysis of the diffraction patterns and identification of the individual peaks, the X-ray diffraction software, HighScore (Malvern Analytical) was used along with the Reitveld analysis for deconvolution of overlapping diffraction peaks.

For microstructural analysis, the Hitachi SU8230 scanning electron microscope (SEM), operating at 10 keV and fitted with a cold field emission gun and Oxford Instruments 150 mm 2 SD energy dispersive X-ray (EDX) detector was used for morphological and phase composition

Table 1

Compositions of brushite (DCPD) and β -calcium pyrophosphate (β -CPP) minerals synthesized using the calcium and iron nitrates and ammonium phosphate solution precursor.

Mineral	Fe%	Theoretical formula
DCPD	0	$\text{CaHPO}_4 \cdot 2\text{H}_2\text{O}$
CPP		β - $\text{Ca}_2\text{P}_2\text{O}_7$
5Fe-DCPD	5	$\text{Ca}_{0.95}\text{Fe}_{0.05}\text{HPO}_4 \cdot 2\text{H}_2\text{O}$
5Fe-CPP		β - $\text{Ca}_{1.9}\text{Fe}_{0.1}\text{P}_2\text{O}_7$
10Fe-DCPD	10	$\text{Ca}_{0.9}\text{Fe}_{0.1}\text{HPO}_4 \cdot 2\text{H}_2\text{O}$
10Fe-CPP		β - $\text{Ca}_{1.8}\text{Fe}_{0.2}\text{P}_2\text{O}_7$
20Fe-DCPD	20	$\text{Ca}_{0.8}\text{Fe}_{0.2}\text{HPO}_4 \cdot 2\text{H}_2\text{O}$
20Fe-CPP		β - $\text{Ca}_{1.6}\text{Fe}_{0.4}\text{P}_2\text{O}_7$
30Fe-DCPD	30	$\text{Ca}_{0.7}\text{Fe}_{0.3}\text{HPO}_4 \cdot 2\text{H}_2\text{O}$
30Fe-FeP		β - $\text{Ca}_{1.4}\text{Fe}_{0.6}\text{P}_2\text{O}_7$

analysis of the initial and the sintered minerals. Prior to SEM analysis, it was necessary to coat the calcium phosphate mineral surface with a 5 nm thin layer of iridium followed by vacuum cleaning for 10 min (Quorum Technologies sputter coater and vacuum cleaner) to minimize electrostatic charging during analysis.

Besides the X-ray powder diffraction and SEM, the attenuated total reflectance ATR-FTIR (Perkin Elmer) was adopted for vibrational spectroscopic characterisation of pressed pellets. This technique is particularly suitable for polycrystalline and IR opaque materials, using which each pellet was scanned over a range of 3000–300 cm^{-1} with spectral resolution of 4 cm^{-1} for analysing the vibrational spectroscopic features of phases formed before and after the heat treatment of doped and undoped DCPD pellet.

Raman spectroscopy is another technique used for the determination of the vibrational spectroscopic structure of the iron-oxide doped calcium phosphate minerals. Raman spectroscopy (Renishaw inVia) with Argon laser at 514 nm with a launch power of ~ 25 mW at the source, which was then reduced to < 10 mW at the objective lens. The vibrational frequency range was from 100 to 2000 cm^{-1} . As in the case of X-ray powder diffraction, in Raman spectroscopy both the crystalline and amorphous structures can be analysed by characterizing the dispersion of vibrational density states.

The mechanical properties of the sintered layers were measured using a NanoTest machine, equipped with a Berkovic indenter (manufactured by Micro Materials Ltd., Wrexham, UK). For each sintered pellet, six hardness measurements at different point with a load of 100 mN were carried out, so that when using the NanoTest software, the derived values for hardness (H, GPa) and Young's Modulus (GPa) can represent a statistical average for the measured data.

2.3. Cell culture

The osteoblasts cell lines G292 (departmental frozen stock) were maintained in alpha minimum essential medium (α -MEM) (Gibco, Life Technologies) supplemented with 10% fetal bovine serum (FBS), 2mM L-glutamine and a penicillin–streptomycin cocktail at 37 °C in an atmosphere of 5% (v/v) CO_2 . The medium was exchanged twice a week until the cells reached 80% confluency.

2.3.1. Contact cytotoxicity assay and extract cytotoxicity assay

Biocompatibility of the pellets was determined using two methods - the contact and extract tests. Samples ($n = 3$ per group) were attached to the centre of six-well tissue culture plates using steir-stripe (3 M Seince). Cyanoacrylate glue and steir-stripe in triplicate were used as positive and negative controls, respectively. G-292 cells were seeded into each well at a density 5×10^3 cells/well (2 mL volume for each well) then incubated at 37 °C in 5% (v/v) CO_2 in air for 48 h. Following incubation, the culture medium was carefully aspirated before the wells were washed with phosphate-buffered saline PBS (calcium and magnesium free) and fixed with 10% (v/v) neutral-buffered formalin (NBF) (Cellpath) for 10 min. The wells were then stained with Giemsa solution (Merck R66 formulation; VWR International, Lutterworth, UK) for five minutes and then repeatedly rinsed with distilled water until clear, after which they were air dried. Changes in cell morphology and confluency were analysed using an Olympus IX 7 inverted microscope under bright field illumination (Cell^B software; Olympus) with all images captured digitally.

Adenosine triphosphates ATP assay (Perkin Elmer kit), which is a common source to detect the living cells in cell culture, was applied as an extract test [20]. Initially, 15 pellet samples (ratio of 3 cm^2/mL ISO10993-12) were incubated in α -MEM with agitation for 72 h at 37 °C. The extract supernatant was collected, checked for sterility and stored at -20 °C until future usage. G292 cell lines, at a density of 5×10^4 cells/200 μl were seeded on 96-well plates and incubated for 24 h. The culture medium was then aspirated and replaced with 20 μl FBS mixed with 180 μl of test extract or controls to the appropriate

wells (in triplicates) and incubated for a further 24 h. Controls included G292 cells cultured in α -MEM as negative control and 40% dimethyl sulfoxide (DMSO) in α -MEM as positive control. The cell viability (relative cellular adenosine triphosphate (ATP) content) was determined using the ATPLite™ assay (Perkin Elmer Life Sciences) following the Perkin Elmer protocols. Eventually, the luminescence was determined using plate reader at a wavelength of 450 nm.

2.3.2. Cell attachment and proliferation

To restrict cells to the surface of pellets during cell seeding, agarose wells of a diameter 1.3 cm were created by pouring 3% of melted agarose in PBS into each well of 12 well plates containing a stainless-steel rod suspended 2 mm above the bottom. After placing the pellets inside the agarose well, 1 mL of media containing 10^4 cell were seeded on the top of each pellet. Cell attachment and proliferation were examined using fluorescence imaging and Picogreen DNA assay.

2.3.3. Fluorescence imaging

After 2 days in culture, cells on pellets were fixed with NBF for 15 min, washed twice with PBS, permeabilised (0.2% by mass Triton X-100 for 5 min) and rinsed three times with PBS. Samples were stained 1 h in PBS with 20 nmol/L Alexa Fluor 546-phalloidin (Invitrogen) and 4',6-diamidino-2-phenylindole DAPI dye (Sigma-Aldrich) to stain for actin and nuclei, respectively. After staining, cells were washed with PBS, air dried and imaged by confocal fluorescence microscopy (Leica TCS SP8).

2.3.4. Picogreen DNA assay

Osteoblast cell line G292 were cultured on pellets and their proliferations was quantified at different times (1 day, 3 days and 7 days) using Picogreen DNA assay (Invitrogen) according to manufacturer's instruction. Briefly, after stipulated time period of incubation, samples were rinsed twice with PBS and subsequently incubated in 300 mL 0.2% Triton in 1x TE buffer (10 mM Tris-HCl, 1 mM EDTA, pH 7.4, (Sigma-Aldrich)) for 15 min. The lysates were then centrifuged at 20,000g for 5 min and DNA content was determined in 100 μl of the supernatants using DNA fluorescence (excitation 480 nm, emission 520 nm) measured using Varioskan Flash plate reader (Thermo Scientific). The data were calibrated using a DNA standard curve.

2.4. Statistical analysis

Quantitative data was analysed using an ANOVA: single factor using a significance level of 5% (P-value of 0.05). All experiments were performed in triplicates, and the data were analysed using Excel Software.

3. Results

3.1. Characterisation results

3.1.1. X-ray powder diffraction

Fig. 1 shows the X-ray powder diffraction patterns of the synthesized minerals. As it was expected, for the undoped DCPD mineral the diffraction peaks at $2\theta = 11.61^\circ, 20.92^\circ, 23.57^\circ, 29.37^\circ$ correspond to the standard brushite (JCPDS-00-011-0293) peaks. The detailed data analysis also confirms the presence of monetite, which was identified by comparing the peaks at $2\theta = 13.06^\circ, 26.40^\circ, 28.49^\circ, 30.46^\circ, 32.50^\circ$ and 32.78° . The Rietveld analysis helped in quantifying the volume fractions of phases present, which was carried out by comparing the intensities of brushite and monetite peaks at 2θ values equal to $11.61^\circ, 20.92^\circ$ and 29.37° , and 26.40° and 28.49° , respectively. From the comparison of the intensities of Bragg peaks, it was estimated that 73.5% of the undoped mineral was brushite and the rest 26.5% monetite. For the 5Fe-DCPD and 10Fe-DCPD synthesized powders, only the brushite phase was identified. However, the diffraction peaks were

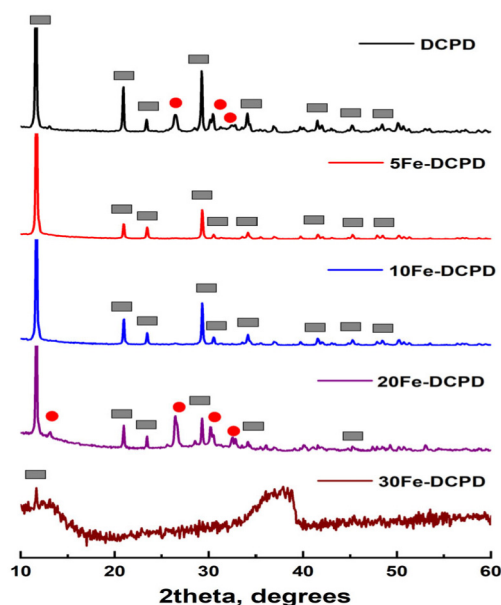


Fig. 1. A comparison of the X-ray diffraction patterns of the synthesized undoped and iron oxide doped minerals, listed in Table 1. (■ for brushite peaks and ● for peaks assigned to monetite).

Table 2

The unit cell parameters of CaP minerals after doping with different concentrations of $\text{Fe}^{2+}/\text{Fe}^{3+}$ -ions.

Materials	a Å	b Å	c Å	V Å ³
DCPD	5.71	15.23	6.09	475.10
5Fe-DCPD	5.70	15.15	6.08	471.01
10Fe-DCPD	5.68	15.04	6.06	463.59
20Fe-DCPD	5.70	15.15	6.08	471.89

found to have shifted to higher angles (from 11.61° to 11.67° and 11.78° in 5Fe-DCPD and 10Fe-DCPD, respectively). The apparent shift in 2θ peaks confirms that the iron ions are incorporated into the crystalline lattice of brushite, which may be better understood by comparing the calculated values of lattice dimensions and cell volumes in Table 2, which were derived from the measured diffraction peaks in Fig. 1.

The observed trend in the reduction in cell volume is expected and it is proportionate with the size of cations, Fe^{2+} and Fe^{3+} , 0.074 and 0.068 nm, which are smaller than that of Ca^{2+} ion at 0.099 nm. As observed in the undoped mineral, in the XRD pattern of the 20Fe-DCPD both the brushite and monetite peaks were identified at a phase volume ratio of 62.9% of brushite to 37.1% of monetite, and these values were ascertained using the Reitveld analysis. Further increase in the doping concentration to 30 mol%, resulted into the formation of an amorphous phase, with only a minor percentage of brushite which was ascertained by identifying the dominant peaks of brushite; e.g. at $2\theta = 11.61^\circ$.

The X-ray powder diffraction patterns of the sintered powders are compared in Fig. 2a. For doping concentrations up to 20 mol%, the heat treated minerals show the dominance of β -CPP, which is identified by the peaks at $2\theta = 26.99^\circ$, 28.97° , 29.66° and 32.62° . At 1000°C , the amorphous 30Fe-DCPD sample transformed into a predominantly crystalline iron phosphate structure (FePO_4) (Fig. 2b) [21].

3.1.2. Fourier transform infrared spectroscopy FTIR

Both the initial and the sintered materials were tested using FTIR (Fig. 3). The initial materials doped with concentrations of Fe-ion up to 20 mol% depict similar reflective spectra as brushite. The vibrational

bands at 873 cm^{-1} , 1124 cm^{-1} and 1211 cm^{-1} were attributed to $(\text{HPO}_4)^{2-}$. The peaks at 524 cm^{-1} , 985 cm^{-1} and 1060 cm^{-1} were assigned to $(\text{PO}_4)^{3-}$. Finally, the band at 1652 cm^{-1} is assigned to the harmonic of OH-ions. The apparent vibrational peaks were found to be consistent with the brushite spectrum, reported elsewhere [22–25]. The vibrational spectrum of 30Fe-DCPD sample corresponds to an amorphous $\text{FePO}_4 \cdot 2\text{H}_2\text{O}$ (Fig. 3a) [26]. The band at 1000 cm^{-1} is assigned to P–O stretching vibration mode while at 1640 cm^{-1} was linked to stretching variation mode of water molecules [21].

In Fig. 3b the FTIR spectrum for the materials after sintering at 1000°C is presented. For doping concentrations to 20 mol%, the presence of β -CPP was confirmed by the P–O–P stretching mode at 723 cm^{-1} . [24,25,27]. By comparison, the presence of crystalline FePO_4 in the sintered 30Fe-DCPD was confirmed by Fe–O stretching vibration modes at 692 cm^{-1} and 628 cm^{-1} [26,28,29].

The FTIR data in Fig. 3a and b clearly show that the as-synthesized mineral powders have strong OH⁻ vibration bands ($1640\text{--}1660\text{ cm}^{-1}$) and in the $2300\text{--}3800\text{ cm}^{-1}$, corresponding to strong OH⁻, weak OH⁻ and free OH bonds. The strength of OH-mineral interaction also depends on the basicity of host mineral and, therefore, depending on the $\text{P}_2\text{O}_5:\text{CaO}$ ratio, the OH⁻ absorption band may shift to high and low energy parts of the IR spectrum. Upon heat treatment, the OH⁻ host bonds break leading to the release of water of crystallization from brushite. The weak and strong bound-OH from monetite are released above 210°C during the heat treatment process [9,30]. Above 500°C , the mineral structure is free from OH⁻ ions (see the absence of $1640\text{--}1660\text{ cm}^{-1}$ and above 3200 cm^{-1} in Fig. 3b), which is why these vibrational bands are absent in the heat treated powder samples.

The temperature dependent phase transformation process, leading to formation of β -CPP is well documented elsewhere [19,31]. When the calcium pyrophosphate minerals are doped with $\text{Fe}^{2+}/\text{Fe}^{3+}$ -ions, the lattice parameter change, as reported in Table 2, as a result of the substitution of Ca^{2+} -ion with the $\text{Fe}^{2+}/\text{Fe}^{3+}$ ions in the crystalline lattice. However, in such a ferrous-ferric ionic substitution, only Fe^{3+} -ions provide complete hybridization of $(\text{PO}_4)^{3-}$ bonds, leaving no excess charge for protonation (H^+), which then leads to less OH⁻ bonds.

The FTIR region between 2000 and 2500 cm^{-1} has several weaker vibration signatures, which correspond to CO_2 and CO_3^{2-} bonds. In the literature of calcium phosphate minerals, there is abundant evidence that during synthesis of phosphates, the CO_2 gas from atmosphere may be absorbed and form carbonate or bicarbonate bonds [32] and such an anionic exchange may then partially replace the phosphate bonds in the structure. The characteristic reduction or disappearance of these bonds in the $2000\text{--}2500\text{ cm}^{-1}$ region also proves that after heat treatment the β -CPP is free from any carbonate bonds.

The FTIR spectra of 30Fe-DCPD mineral before and after heat treatment shows that large fraction of this mineral remains less crystalline than other compositions, listed in Table 1. It is evident from the lack of sharply defined vibrational bands in the 500 to 1250 cm^{-1} , which is where the crystalline phosphates structures have clearly defined vibrational modes as shown in Fig. 3a and b. Table 3 presents the vibrational functional groups in IR and Raman of DCPD, amorphous $\text{FePO}_4 \cdot 2\text{H}_2\text{O}$, β -CPP and FePO_4 .

3.1.3. Raman spectroscopy

Raman spectroscopy was also used to confirm crystallinity of samples. For DCPD, 5Fe-DCPD, 10Fe-DCPD and 20Fe-DCPD, the main Raman peak for the $(\text{PO}_4)^{3-}$ symmetric stretching modes were observed, as can be seen in Fig. 4a at 988 cm^{-1} . The peak at 1147 cm^{-1} is assigned to the antisymmetric stretching mode of HPO_4^{2-} . The bands at 420 cm^{-1} and 385 cm^{-1} were attributed to symmetric bending mode PO_4^{3-} in the brushite phase as shown in Table 3. At relatively small doping concentrations of iron ions in 5Fe- and 10Fe-DCPD, the brushite structure did not modify. However, the intensity of Raman scattering increased in comparison with the undoped DCPD mineral, which may signify an increase in crystallinity of the material, as was also confirmed

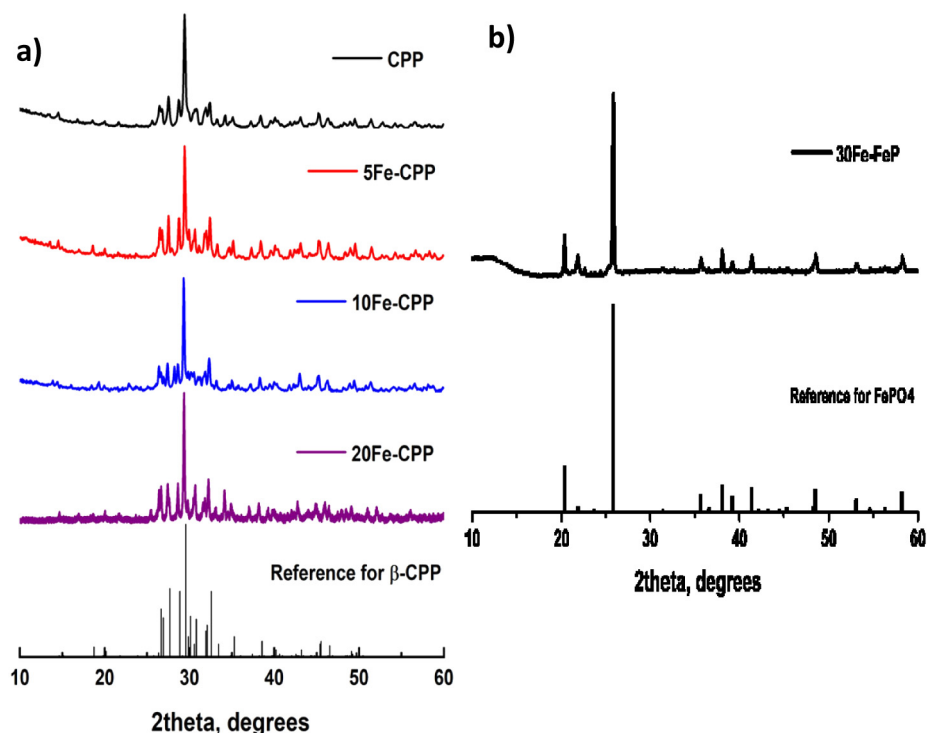


Fig. 2. A comparison of the X-ray diffraction peaks of iron oxide doped CaP powders sintered at 1000 °C for 5 h in air of a) 0, 5, 10 and 20Fe-DCPD powders demonstrates a β -CPP phase, in the agreement of the JCPDS file (00-033-0297). b) 30Fe-CaP transformed into FePO_4 as reported in the JCPDS (04-012-1439).

with XRD. Although there was no change in the position of the main peaks for 20Fe-DCPD, the dominant peak at around 1000 cm^{-1} was found to be relatively broader in comparison with the powder samples of 5Fe- and 10Fe-DCPD. The broadness of the dominant peak defines the loss of the continuum of vibrational modes which are quantum confined due to the 3-dimensional periodicity of crystalline lattice.

For 30Fe-DCPD, the main peak appeared to have shifted to a higher wavenumber at 1009 cm^{-1} than that in the DCPD, indicating that the relatively higher iron concentration may have led to a change in the local calcium phosphate structure of DCPD, as can be compared in Fig. 4a. The Raman and FTIR vibrational analyses also confirm the phase transformation reaction. The main peak at 1009 cm^{-1} is

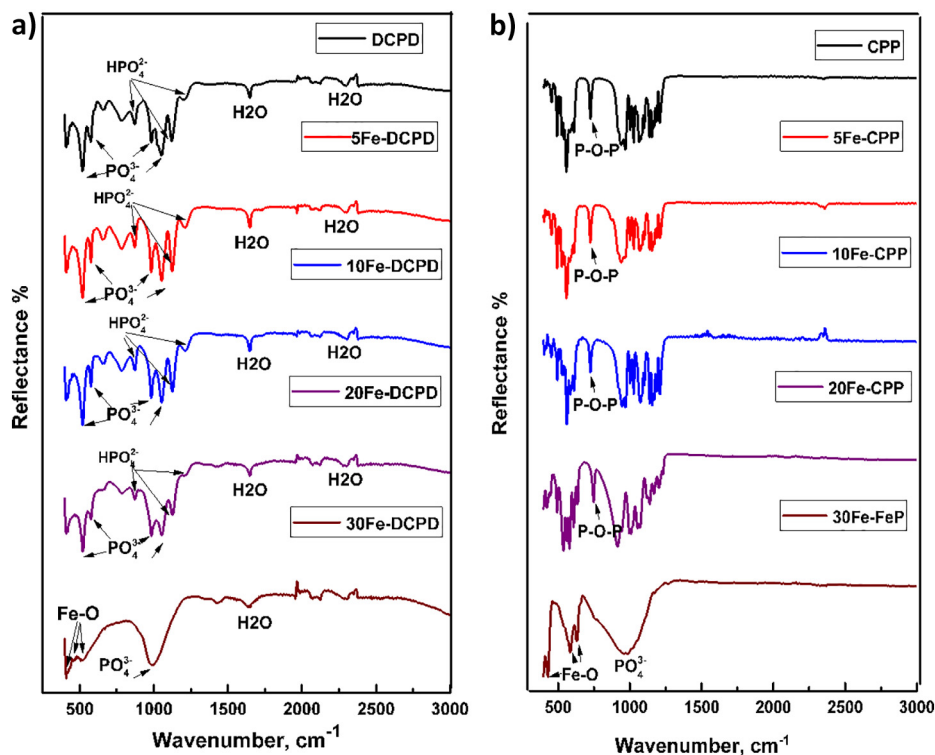


Fig. 3. ATR-FTIR spectrum of the a) synthesized and b) sintered powders 0, 5, 10, 20 and 30 mol% of $\text{Fe}^{2+}/\text{Fe}^{3+}$ ion.

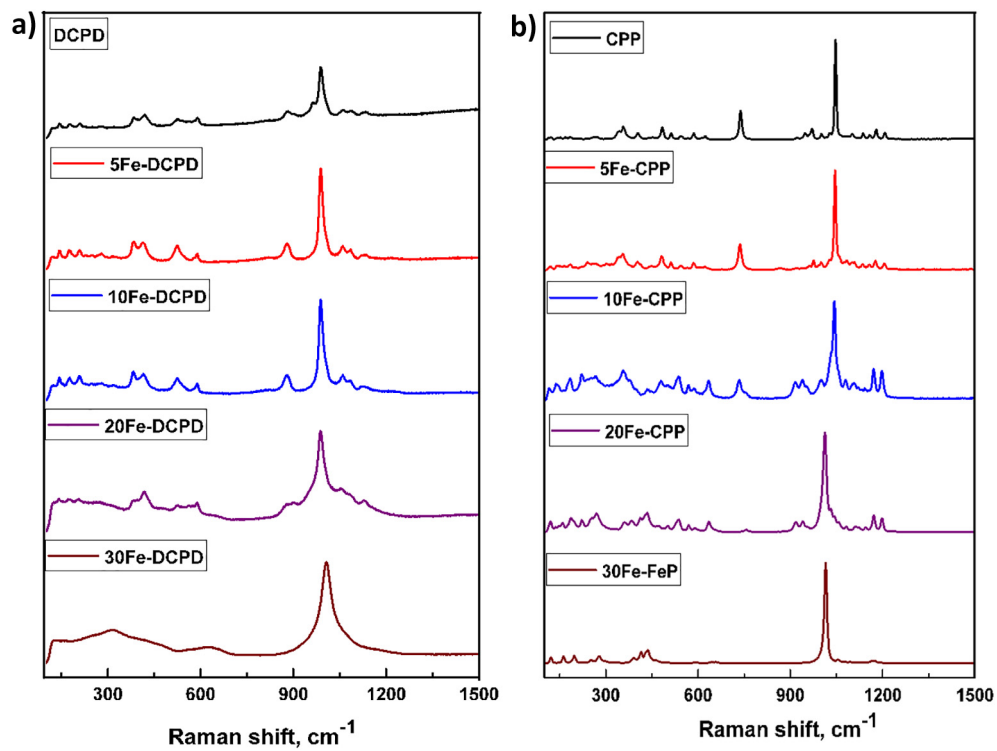


Fig. 4. Raman spectrum of the a) synthesized and b) sintered powders 0, 5, 10, 20 and 30 mol% of $\text{Fe}^{2+}/\text{Fe}^{3+}$ ion.

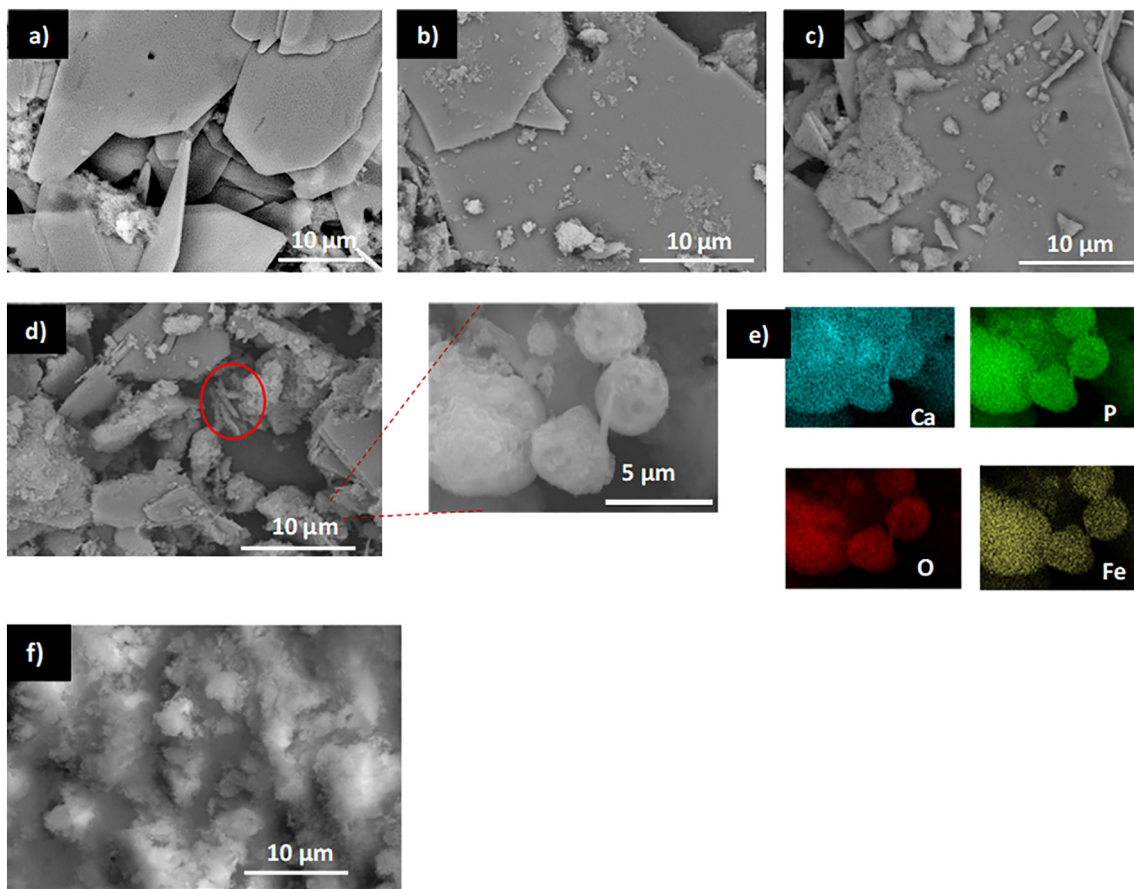


Fig. 5. SEM images of the brushite (platelets) and monetite (needle-like, red circle) crystals formed during synthesis of; a) DCPD; b) 5Fe-DCPD; c) 10Fe-DCPD; d) 20Fe-DCPD; e) EDX maps of the inset of 20FeCaP mineral indicates iron phosphate particles; and f) for 30Fe-DCPD. (For interpretation of the references to colour in this figure legend, the reader is referred to the web version of this article.)

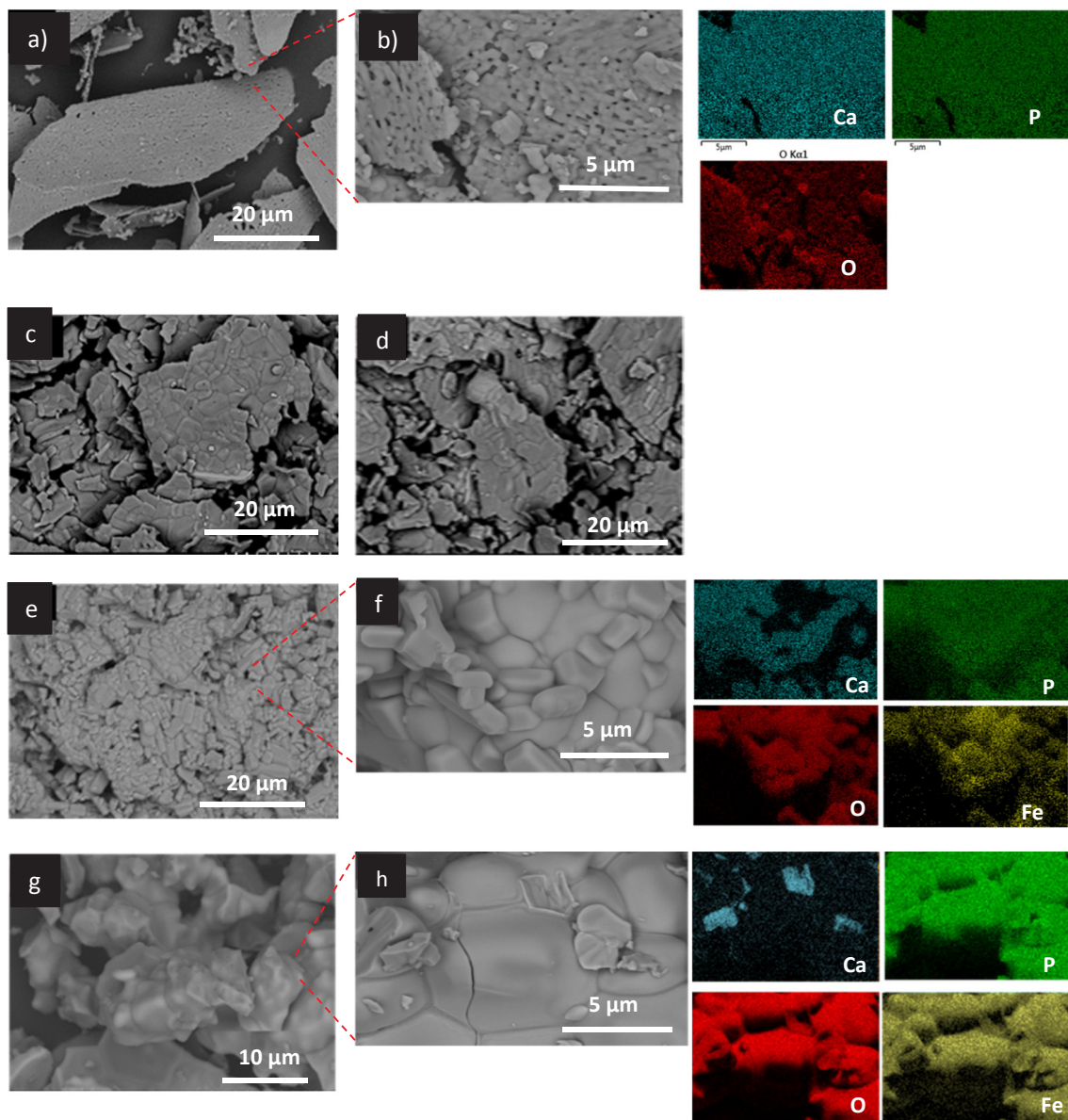


Fig. 6. SEM images of a), b) of CPP and its EDX map, c) 5Fe-CPP, d) 10Fe-CPP, e), f) 20Fe-CPP and its EDX map and g), h) 30Fe-FeP and its EDX map at 1000 °C for 5 h show the morphology and element compositions of each material.

3.1.5. Mechanical properties

After structural and microstructural characterisation discussed above, the effect of iron doping on the mechanical properties of the densified brushite (DCPC) after heat treatment at 1000 °C was investigated by characterizing the hardness and Young's modulus of powder pressed pellets, discussed above. Since brushite loses 2.5 molecules of water while reaching sintering temperature at 1000 °C, there is a reduction in 23% weight loss in molar mass. The loss in weight is manifested in the generation of a porous microstructure, as can be seen in Fig. 6a, which at elevated temperature leads to progressive increase in the density of pressed powder pellets. The effect of isothermal heat treatment of undoped and iron oxide ($\text{Fe}^{2+}\backslash\text{Fe}^{3+}$) doped pellets at 1000 °C for 5 h result into a systematic increase in the density of pellets. The apparent increase in the densities of sintered pellets are compared in Fig. 7a, in which the values of percentage increase are 5.4%, 22.5%, 30.2% and 33.2% for the 5Fe-CPP, 10 Fe-CPP, 20 Fe-CPP and 30Fe-FeP pellets, respectively.

After densification, the hardness and Young's modulus were measured using the nano-indentation technique, discussed above, and the

results are compared in Table 4. The data for hardness and Young's modulus measurements for undoped DCPD before and after densification do not demonstrate much difference, as shown in Fig. 7b. In 5, 10, and 20 mol% iron oxide doped mineral pellets, there is a systematic increase in the values of measured hardness and Young's modulus, as compared in Table 4. Although the measured values of hardness reach maximum at 10 mol% iron oxide doping, by comparison the highest value of Young's modulus is observed for 20 mol% doped DCPD. Amongst the 5 different mineral compositions investigated for the characterisation mechanical properties, the 30 mol% iron oxide pellets have the lowest values of hardness and Young's modulus, in spite of the fact this composition demonstrated the highest increase in the density, when compared with other pellets.

3.2. Evaluation of biocompatibility and cell growth

In vitro evaluation of the effects of cytotoxicity of sintered undoped and iron oxide doped calcium phosphate (CaP) minerals on G292 cells culture was investigated by undertaking both the contact and extract

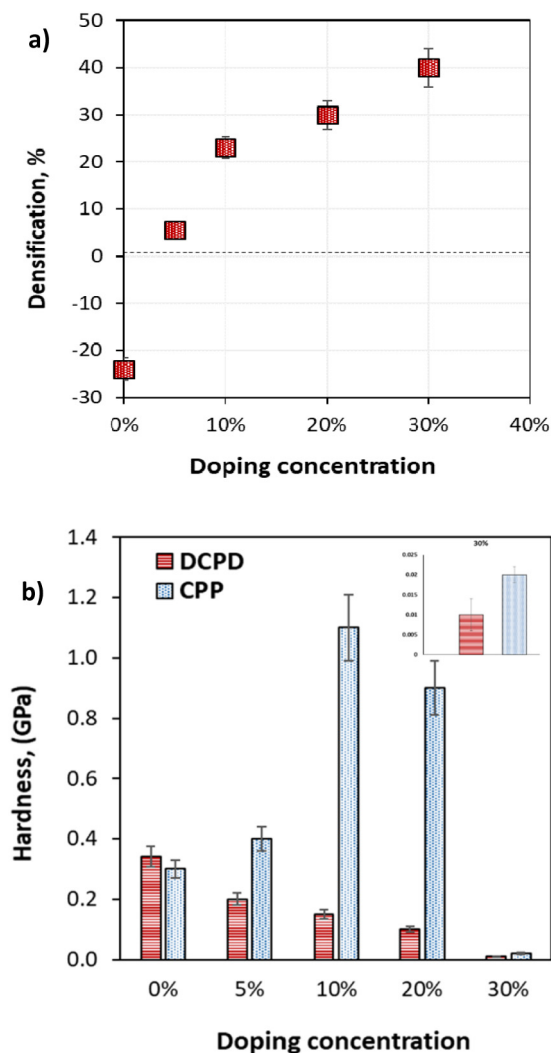


Fig. 7. a) Densification of the minerals after sintering; b) Nano-hardness of FeCaP samples at load of 100 mN where the inset shows the hardness value of 30% sample. Error bars present standard deviation.

Table 4
Mechanical properties of the initial and sintered FeCaP minerals.

Materials	Hardness (GPa)		Young's modulus (GPa)	
	DCPD	CPP	DCPD	CPP
0-FeCaP	0.34 ± 0.03	0.3 ± 0.05	7.84 ± 0.4	7.7 ± 0.5
5-FeCaP	0.2 ± 0.02	0.4 ± 0.07	5.86 ± 0.4	6.4 ± 0.4
10-FeCaP	0.15 ± 0.04	1.1 ± 0.4	3.6 ± 0.6	10.5 ± 1.0
20-FeCaP	0.1 ± 0.02	0.9 ± 0.3	3.1 ± 0.3	13.3 ± 2.6
30-FeCaP	0.01 ± 0.002	0.02 ± 0.003	0.3 ± 0.2	1.2 ± 0.07

assays. In contact assay, the microscopic analysis of cell culture of iron oxide doped and undoped CaP mineral samples showed similar results to that of the control. There was no evidence for cytotoxicity as verified by the G292 culture presented neither zones of morphological change, nor the cell lysis were noted. The evidence for cell growth in contact with the pellet samples of CPP, 5Fe-CPP, 10Fe-CPP, 20Fe-CPP and 30Fe-FeP are compared in Fig. 8a, c, d, e, f and g, whereas the cyanoacrylate glue (positive control) resulted in dramatic decrease of cell density as well as dead cells, as shown in Fig. 8b.

In the Extract Cytotoxicity Assay, there was no significant reduction in the cellular ATP levels of the G292 cells following incubation with soluble extracts of CPP, 5Fe-CPP, 10Fe-CPP, 20Fe-CPP and 30Fe-FeP

samples compared with that of the DMEM (negative control) ($P > 0.05$). While the positive controls, 40% dimethyl sulfoxide (DMSO) caused an almost total loss of ATP (Fig. 9) as it was significantly different in comparison with the negative control ($P < 0.05$).

Quantitative and qualitative approaches for cell growth on the top of CPP, 5Fe-CPP, 10Fe-CPP, 20Fe-CPP and 30Fe-FeP pellets were also investigated. For the qualitative test, the confocal microscopic examinations of cell growth were carried out after 48 h.

The results of cell attachment and proliferation on the top of pellets are compared in Fig. 10 for undoped and iron oxide doped minerals.

For determining the optimal concentrations of iron oxide for the proliferation of osteoblast cells, a quantitative approach by counting the number of cells on mineral surface was adopted by following pi-cogreen protocol for different intervals (1, 3 and 7 days).

In Fig. 11, the DNA content of cells after incubation with the materials for 1 day shows a sharp increase in the statistically significant proliferation activity ($P < 0.05$) in all iron oxide doped mineral samples. The data on proliferation show that the maximum value was reached after 3 days, after which the proliferation activities (7 days) in all mineral samples started diminishing ($P < 0.05$).

4. Discussion

In this investigation, the aspects of materials engineering and characterisation of $\text{Fe}^{2+,3+}$ -doped β -CPP as a novel bone material appears to fulfil two out of four requirements which have been identified in the Diamond Concept [3]. The osteogenic properties of $\text{Fe}^{3+,2+}$ -doped β -CPP were investigated and it was demonstrated that the heat-treated minerals support osteoblast attachment and proliferation (shown in Figs. 8, 10 and 11). The mineral cell support does not induce any toxicity, as demonstrated by the ATP assay analysis in Fig. 9.

The supporting evidence for favourable osteogenic host environment is essential along with the load-bearing properties and sustainability of angiogenesis across the damaged bone. In the early healing phase, the biomechanical compatibility of an implant plays an important role with natural bone for osteogenesis which relies on nutrient and blood flow [11,19]. In this investigation, the comparison of cell proliferation properties with the characterisation of mechanical properties clearly demonstrates that the 10 mol% iron oxide doped sintered mineral exhibits much improved hardness and Young's modulus properties (shown in Table 4); for example from 0.4 GPa in undoped materials to ~ 1.1 GPa in 10Fe-DCDP minerals after sintering. For minerals doped with iron oxide beyond 10 mol% (e.g. 20Fe-DCDP) the hardness and modulus values are higher than that for 10Fe-DCDP. These materials on sintering and load bearing exhibit cracks and, therefore, depict brittleness when compared with 10Fe-DCDP. However, the osteoblast growth and ATP assay data analysed confirmed that in these two compositions, 10Fe-DCDP and 20Fe-DCDP, the overall cell compatibility behaviour is comparable within the limits of data analysis.

The structural mechanism of doping iron ions in DCDP has been proven and occurs as a result of ionic substitution of Ca^{2+} ions in the DCDP structure with the ferric/ferrous ions in the synthesized and sintered minerals. The cationic substitution is possible because the ionic radii of $\text{Fe}^{3+}/\text{Fe}^{2+}$ ions (0.074/0.068 nm) are comparable with that for Ca^{2+} (0.099 nm), which is based on the crystal chemistry of calcium ferrite and CaO-FeO phase diagrams that both the ferric and ferrous states substitute Ca^{2+} -ions and form complexes with terminal solid solutions [38,39]. A similar trend for solid solution formation with DCDP and β -CPP has been observed before and after sintering, respectively, which were confirmed with the changes in the positions of the Bragg reflections in X-ray powder diffraction and crystal cell volume calculations in Table 2, shapes of the vibrational peaks in FTIR and Raman spectra, discussed above, in Figs. 3a-b and Fig. 4a-b, respectively. As the doping concentration of iron oxide is increased beyond 10 mol%, the presence of FePO_4 became apparent, and the change

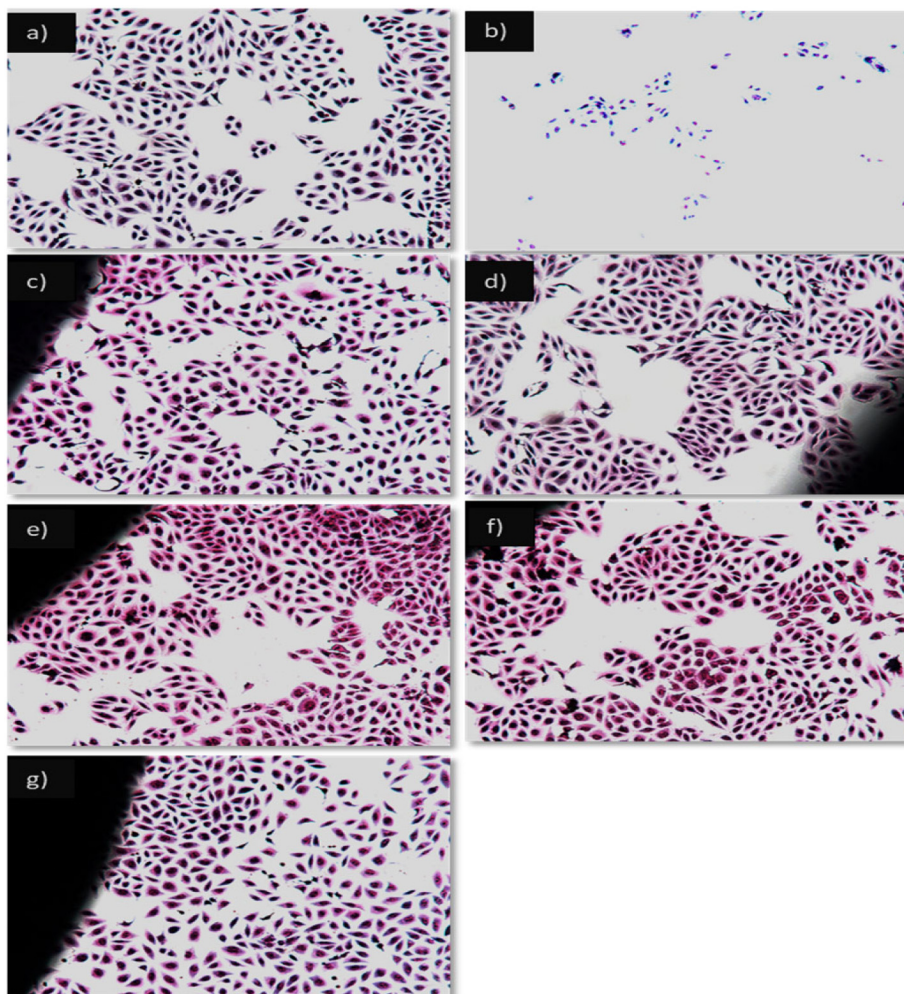


Fig. 8. Contact test of a) negative and b) positive controls in comparison to c) CPP, d) 5Fe-CPP, e) 10Fe-CPP, f) 20Fe-CPP and g) 30Fe-FeP sintered pellets seeded with osteoblast cell line.

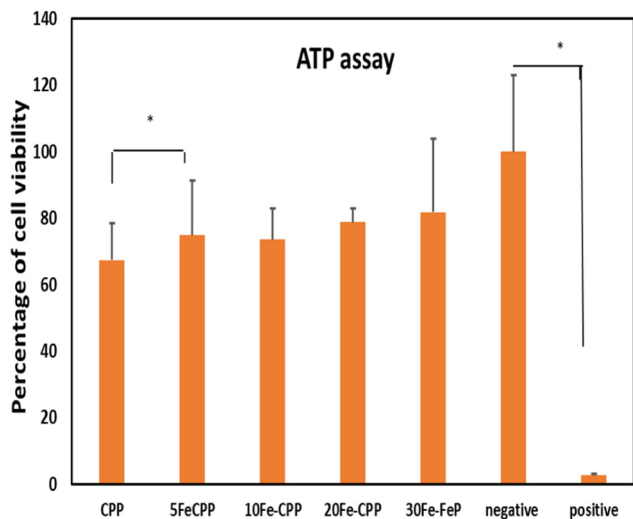


Fig. 9. Cell viability of sintered samples in comparison to negative and positive controls using ATP assay, (*) illustrates significant difference ($P < 0.05$).

in the composition increased the number of iron bonds with $(\text{PO}_4)^{3-}$ groups at the Ca^{2+} ionic sites. Consequently, due to increasingly strong presence of 3^+ ionic vibrational bands at the cationic sites in the DCDP, the number of Ca^{2+} -ion link with phosphate reduces with cationic

substitution. Above 20 mol% ferric-ferrous substitution, the DCDP crystalline phase begins to amorphise, which is evident from the line broadening of the Bragg reflection and the Raman scattering peaks, in Figs. 2 and 4, respectively. Although the precise mechanism of amorphization is still under investigation, the apparent change in the crystalline phase combination with the preponderance of FePO_4 in the sintered material suggests that before sintering the constituents of FePO_4 phase do not interact with the DCDP in the solution phase due to the change in pH, which prevents the formation of crystalline phase. By contrast, during sintering the amorphous phase is only prevalent at low temperatures, and the complex iron-calcium crystalline phosphate phase forms as verified by the lattice parameter analysis in Table 2. For obtaining β -CPP phase, the minerals were sintered at 1000°C for 5 h for promoting the phase transformation of brushite into the β -CPP, which was dominated in compositions up to 20Fe-DCDP. By comparison. In 30Fe-DCPD the phase transformation at 1000°C yielded crystalline FePO_4 , as shown in Figs. 2–4 in the X-ray powder diffraction, FTIR and Raman spectra. The transition from crystalline to amorphous phase is a subject of more detailed analysis and will be discussed in future in another article.

The densification of ceramic during sintering process [40] is defined by the reduction in the porosity, which is evident from the comparison of detailed SEM images, presented in Fig. 5a–g and Fig. 6a–g. For undoped mineral the structure showed a large number of porosities along the surface of the crystalline β -CPP (see Fig. 6a) that appeared after sintering. The presence of such a large number of intra planar porosities

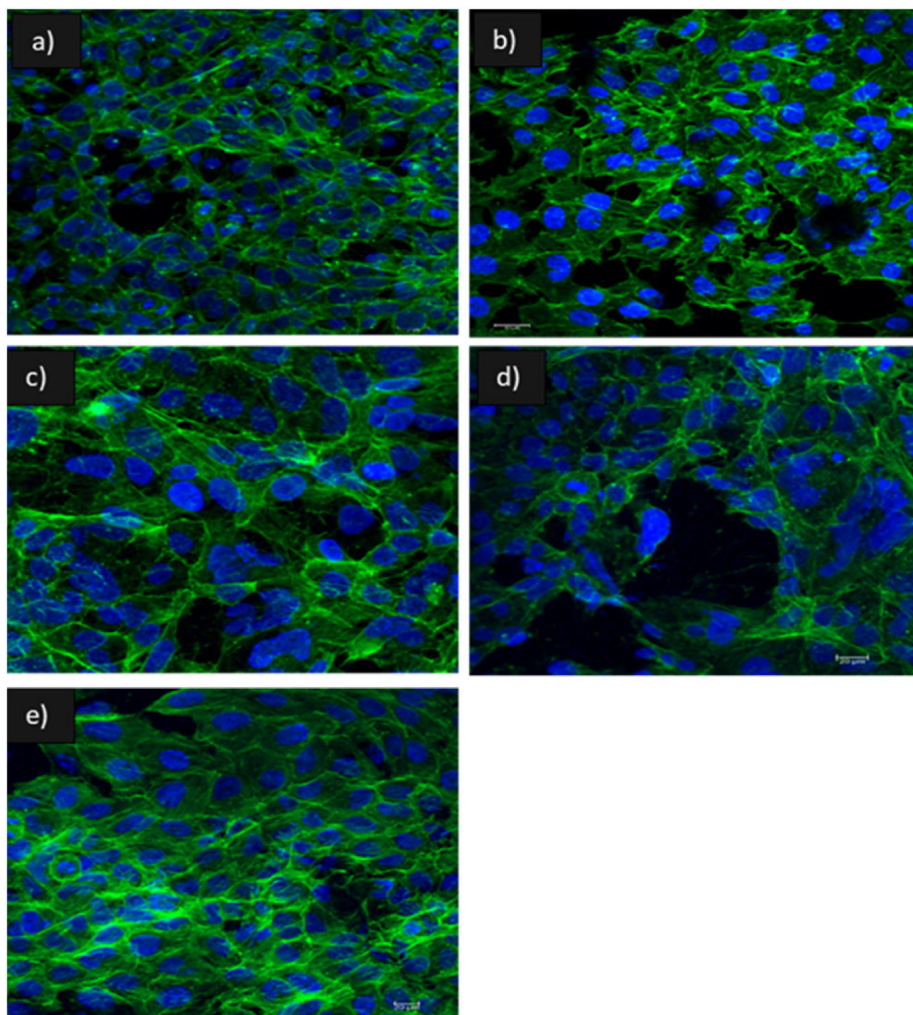


Fig. 10. Confocal microscopy of cell growth on sintered pellet samples a) CPP, b) 5Fe-CPP, c) 10Fe-CPP, d) 20Fe-CPP and e) 30Fe-FeP after seeding with osteoblast cells for 48 h, scale bar 50 μm .

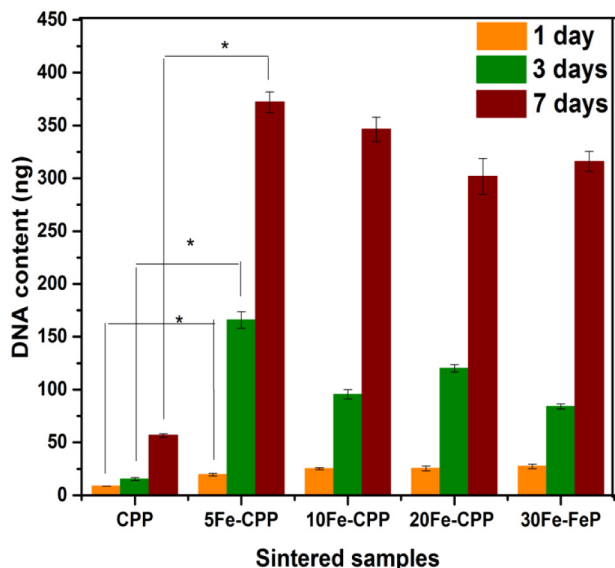


Fig. 11. Proliferation results after 1, 3 and 7 days for CPP, 5Fe-CPP, 10Fe-CPP, 20Fe-CPP and 30Fe-FeP,* illustrates a significant difference ($P < 0.05$).

act as defects for crack propagation and reduce the hardness and Young's modulus [41]. However, doping with iron decreases the porosity by making DCDP less stable in preference with complex β -CPP. The presence of β -CPP increases grain growth because of the solid-solution formation between β -CPP and FePO_4 , leading to lattice induced mass transport for grain growth [42]. With increasing volume fraction of FePO_4 , the complex microstructure with a mixture of amorphous and crystalline phases becomes more brittle, as the microstructural feature for crack attenuation becomes less prevalent.

Biocompatibility for cytotoxicity assay (contact and extract) shows that the materials were not toxic. The ATP assay using samples extractions showed a reduced number of viable cells and a lower cell density on CPP, when compared with the samples doped with iron oxide. Xia et al. [43], suggested that Fe ions might increase the occurrence of protein that is responsible for cell adhesion, thus more cells adheres to Fe-doped β -CPP, in comparison to the undoped mineral.

The microstructure and surface morphology also have an impact on cell behaviour, it was found that the sintered Fe-DCDP scaffolds with porous structure attracts more cells than the samples with large crystalline structures [25]. Furthermore, Fe^{3+} -ion also plays an essential role in transferring oxygen through haemoglobin in blood [44]. Zhang et al. [45] demonstrated that octacalcium phosphate doped with iron ions (Fe-OCP) can enhance angiogenesis and, therefore, the presence of iron ions in β -CPP may have a favourable effect on the cell proliferation behaviour [46]. In general, the 10Fe-CPP mineral substrate shows good

results both in terms of mechanical and biological properties. This makes it a promising material for the fabrication of bone scaffolds where a combination of both the mechanical stability and enhanced regenerative potential may be required.

5. Conclusions

In this work, the β -CPP mineral with various doping concentrations of iron oxide were prepared and both the osteogenic and mechanical properties were investigated in detail for engineering materials that may be used in the fabrication of bone scaffolds. The findings of our work are summarised below.

- i) It has been demonstrated that in undoped calcium phosphate minerals, the dominant phase is the brushite ($\text{CaHPO}_4 \cdot 2\text{H}_2\text{O}$) which is the dominant phase also in the minerals doped with 5–20 mol% concentrations of iron oxide. When the doping concentrations reach at and above 20 mol%, there is evidence for the presence of an amorphous phase which is constituted of $\text{FePO}_4 \cdot 2\text{H}_2\text{O}$ and brushite. For higher concentrations the tendency for amorphization increases during materials synthesis.
- ii) The heat treatment of undoped and iron doped brushite for 5 h at 1000 °C in air yields a combination of phases, and depending on iron oxide concentrations, the dominant phase below 20 mol% is β -CPP. As the concentration reaches above 20 mol%, the phase combination changes from β -CPP to FePO_4 and a small fraction of amorphous phase. At 30 mol%, the phase transformation yields dominant FePO_4 and traces of remaining amorphous phase, as confirmed by X-ray powder diffraction, Raman and FTIR spectroscopy.
- iii) The iron oxide doped sintered pellets were tested for cell viability and proliferation which were analysed using ATP assay analysis and optical microscopy, respectively. It was found that the presence of iron oxide increases the osteogenic properties which peaks between 10 mol% and 20 mol% of $\text{Fe}^{2+}/\text{Fe}^{3+}$ ions in β -CPP. Above this concentration the osteogenic response was much poorer.
- iv) The sintered mineral pellets were also tested for the characterisation of Young's modulus and hardness, and from the results it was established that 10 mol% and 20 mol% $\text{Fe}^{2+}/\text{Fe}^{3+}$ ions sintered pellets depict much higher values of hardness and Young modulus than the sintered pellets beyond this composition range. The samples above 20 mol% iron oxide were found to be more brittle due to the prevalence of amorphous phase.
- v) On the basis of mechanical properties and osteogenic growth potential analysis, it was concluded that the 10 mol% iron oxide containing β -CPP is likely to be optimal candidate for bone scaffold engineering for replacing HAP.

Author contributions

Emaan Alsubhe undertook research and generated research data, presented herein. AA, as a Senior Research Fellow, trained EA in the areas of methodologies of materials preparation and characterisations, using X-ray powder diffraction, spectroscopic and thermal analysis techniques. She also analysed the data under the supervisions of the academic supervisors, named above as the co-authors (EMR, AH, PVG and AJ). EMR supervised and helped in the planning and characterisation of cell toxicity and proliferation tests. AH was responsible for the supervision of mechanical testing which involved training EA in undertaking measurements using the Berkovic indenter. MM supported EA in the areas of sample preparation and data processing of nano indentation measurements. AJ and PG supervised the research on bone materials for scaffold engineering. Both reviewed and helped in undertaking major revision of the article with the support from EA and AA.

Declaration of competing interest

The authors declare that they have no known competing financial interests or personal relationships that could have appeared to influence the work reported in this paper.

Acknowledgements

The authors acknowledge Taibah University (Saudi Arabia) for the financial support and the University of Leeds (Leeds, UK) for supporting this project. The authors also acknowledge the support from the CiC-MRC (University of Leeds), Innovate UK (TS/S002022/1, TS/L004070/1), EU-MarieCurie-IIF (Pre-FaCTO,660147) EPSRC (UK) (EP/K020234/1) projects. Also, the authors would like to acknowledge Dr. Sarah Myers, Mr. Mohammed Javed and Mr. Stuart Micklethwaite for their laboratory help.

Appendix A. Supplementary data

Supplementary data to this article can be found online at <https://doi.org/10.1016/j.msec.2020.111053>.

References

- [1] D. Toroian, J.E. Lim, P.A. Price, The size exclusion characteristics of type I collagen implications for the role of noncollagenous bone constituents in mineralization, *J. Biol. Chem.* 282 (2007) 22437–22447, <https://doi.org/10.1074/jbc.M700591200>.
- [2] LeGeros, R.Z., Properties of osteoconductive biomaterials: calcium phosphates. *Clin. Orthop. Relat. Res.* 395 (2002) 81–98, https://journals.lww.com/clin-orthop/Fulltext/2002/02000/Properties_of_Osteoconductive_Biomaterials__9.aspx.
- [3] P.V. Giannoudis, T.A. Einhorn, D. Marsh, Fracture healing: the diamond concept, *Injury* 38 (2007) S3–S6, [https://doi.org/10.1016/S0020-1383\(08\)70003-2](https://doi.org/10.1016/S0020-1383(08)70003-2).
- [4] G. Bosch, et al., The effect of platelet-rich plasma on the neovascularization of surgically created equine superficial digital flexor tendon lesions, *Scandinavian J Medicine & Science of Sports* 21 (2011) 554–561, <https://doi.org/10.1111/j.1600-0838.2009.01070.x>.
- [5] Stewart, S.J.M.o.j., Fracture non-union: a review of clinical challenges and future research needs. *Malaysian Orthopaedics Journal*. 13 (2019) 1, <https://www.ncbi.nlm.nih.gov/pmc/articles/PMC6702984/>.
- [6] J.C. Silva, et al., Extracellular matrix decorated polycaprolactone scaffolds for improved mesenchymal stem/stromal cell osteogenesis towards a patient-tailored bone tissue engineering approach, *J. Biomed. Mater. Res. B Appl. Biomater.* (2020), <https://doi.org/10.1002/jbm.b.34554>.
- [7] T. Aghaloo, et al., The effects of systemic diseases and medications on implant osseointegration: a systematic review, *International Journal of Oral & Maxillofacial Implants* 34 (2019), <https://doi.org/10.11607/jomi.19suppl.g3>.
- [8] W. Habraken, et al., Calcium phosphates in biomedical applications: materials for the future? *Mater. Today* 19 (2016) 69–87, <https://doi.org/10.1016/j.mattod.2015.10.008>.
- [9] A. Anastasiou, et al., Exogenous mineralization of hard tissues using photo-absorptive minerals and femto-second lasers; the case of dental enamel, *Acta Biomater.* 71 (2018) 86–95, <https://doi.org/10.1016/j.actbio.2018.02.012>.
- [10] A. Anastasiou, et al., β -Pyrophosphate: a potential biomaterial for dental applications, *Mater. Sci. Eng. C* 75 (2017) 885–894, <https://doi.org/10.1016/j.msec.2017.02.116>.
- [11] A. Manchón, et al., A new iron calcium phosphate material to improve the osteoconductive properties of a biodegradable ceramic: a study in rabbit calvaria, *Biomed. Mater.* 10 (2015), <https://doi.org/10.1088/1748-6041/10/5/055012>.
- [12] S. Panseri, et al., Intrinsically superparamagnetic Fe-hydroxyapatite nanoparticles positively influence osteoblast-like cell behaviour, *Journal of nanobiotechnology* 10 (2012) 32, <https://doi.org/10.1186/1477-3155-10-32>.
- [13] W. Liu, et al., Novel tricalcium silicate/magnesium phosphate composite bone cement having high compressive strength, in vitro bioactivity and cytocompatibility, *Acta Biomater.* 21 (2015) 217–227, <https://doi.org/10.1016/j.actbio.2015.04.012>.
- [14] Y.J. No, S.-i. Roohani-Esfahani, H. Zreiqat, Nanomaterials: the next step in injectable bone cements, *Nanomedicine* 9 (2014) 1745–1764, <https://doi.org/10.2217/nmm.14.109>.
- [15] B. Kanter, et al., Bone regeneration capacity of magnesium phosphate cements in a large animal model, *Acta Biomater.* 69 (2018) 352–361, <https://doi.org/10.1016/j.actbio.2018.01.035>.
- [16] J. Zheng, et al., Fabrication and characterization of a novel carbon fiber-reinforced calcium phosphate silicate bone cement with potential osteo-inductivity, *Biomed. Mater.* 11 (2015) 015003, <https://doi.org/10.1088/1748-6041/11/1/015003>.
- [17] Lin, F.-H., et al., Mechanical properties and histological evaluation of sintered β -Ca₂P₂O₇ with Na₄P₂O₇ 10H₂O addition. *Biomaterials*. 16 (1995) 793–802, <http://www.sciencedirect.com/science/article/pii/014296129599642Y>.
- [18] Grover, L.M., et al., The effect of amorphous pyrophosphate on calcium phosphate

- cement resorption and bone generation. *Biomaterials*. 34 (2013) 6631–6637, <http://www.sciencedirect.com/science/article/pii/S0142961213005413>.
- [19] A. Anastasiou, et al., Sintering of calcium phosphates with a femtosecond pulsed laser for hard tissue engineering, *Mater. Des.* 101 (2016) 346–354, <https://doi.org/10.1016/j.matdes.2016.03.159>.
- [20] R. Mempo, et al., Release of extracellular ATP by bacteria during growth, *BMC Microbiol.* 13 (2013) 301, <https://doi.org/10.1186/1471-2180-13-301>.
- [21] C.-T. Hsieh, et al., Synthesis of iron phosphate powders by chemical precipitation route for high-power lithium iron phosphate cathodes, *Electrochim. Acta* 83 (2012) 202–208, <https://doi.org/10.1016/j.electacta.2012.07.108>.
- [22] S. Singh, et al., Synthesis of brushite nanoparticles at different temperatures, *Chem. Pap.* 64 (2010) 491–498, <https://doi.org/10.2478/s11696-010-0032-8>.
- [23] S. Mandel, A.C. Tas, Brushite (CaHPO₄·2H₂O) to octacalcium phosphate (Ca₈(HPO₄)₂(PO₄)₄·5H₂O) transformation in DMEM solutions at 36.5 °C, *Mater. Sci. Eng. C* 30 (2010) 245–254, <https://doi.org/10.1016/j.msec.2009.10.009>.
- [24] T. Corrêa, J. Holanda, Calcium pyrophosphate powder derived from avian eggshell waste, *Cerâmica* 62 (2016) 278–280, <https://doi.org/10.1590/0366-69132016623631986>.
- [25] S.R. Vasant, M. Joshi, Synthesis and characterization of nanoparticles of calcium pyrophosphate, *Modern Physics Letters B* 25 (2011) 53–62, <https://doi.org/10.1142/S0217984911025419>.
- [26] B.M. Al-Hasni, G. Mountjoy, E. Barney, A complete study of amorphous iron phosphate structure, *J. Non-Cryst. Solids* 380 (2013) 141–152, <https://doi.org/10.1016/j.jnoncrysol.2013.08.031>.
- [27] R. Mulongo-Masamba, et al., Synthesis and thermal dehydroxylation kinetic of anhydrous calcium phosphate monetite CaHPO₄, *J. Therm. Anal. Calorim.* 124 (2016) 171–180, <https://doi.org/10.1007/s10973-015-5130-y>.
- [28] B. Boonchom, S. Puttawong, Thermodynamics and kinetics of the dehydration reaction of FePO₄·2H₂O, *Phys. B Condens. Matter* 405 (2010) 2350–2355, <https://doi.org/10.1016/j.physb.2010.02.046>.
- [29] S. Okada, et al., Cathode properties of amorphous and crystalline FePO₄, *J. Power Sources* 146 (2005) 570–574, <https://doi.org/10.1016/j.jpowsour.2005.03.200>.
- [30] A. Anastasiou, et al., Drug loading capacity of microporous β-pyrophosphate crystals, *Mater. Des.* 168 (2019), <https://doi.org/10.1016/j.matdes.2019.107661>.
- [31] N.W. Wikholm, R.A. Beebe, J.S. Kittelberger, Kinetics of the conversion of monetite to calcium pyrophosphate, *J. Phys. Chem.* 79 (1975) 853–856, <https://doi.org/10.1021/j100575a017>.
- [32] S. Lala, et al., Magnesium substitution in carbonated hydroxyapatite: structural and microstructural characterization by Rietveld's refinement, *Mater. Chem. Phys.* 170 (2016) 319–329, <https://doi.org/10.1016/j.matchemphys.2015.12.058>.
- [33] C.-L. Li, B. Zhang, Z.-W. Fu, Physical and electrochemical characterization of thin films of iron phosphate and nitrided iron phosphate for all-solid-state batteries, *J. Electrochem. Soc.* 153 (2006) E160–E165, <https://doi.org/10.1149/1.2218110>.
- [34] B.C. Cornilsen, Solid state vibrational spectra of calcium pyrophosphate dihydrate, *J. Mol. Struct.* 117 (1984) 1–9, [https://doi.org/10.1016/0022-2860\(84\)87237-3](https://doi.org/10.1016/0022-2860(84)87237-3).
- [35] D. De Waal, C. Hutter, Vibrational spectra of a solid solution of cadmium and calcium pyrophosphate, *Mater. Res. Bull.* 29 (1994) 1129–1135, [https://doi.org/10.1016/0025-5408\(94\)90182-1](https://doi.org/10.1016/0025-5408(94)90182-1).
- [36] B. Cornilsen, R.J.J. Condrate Sr., N. Chemistry, The vibrational spectra of β-Ca₂P₂O₇ and γ-Ca₂P₂O₇, *J. Inorg. Nucl. Chem.* 41 (1979) 602–605, [https://doi.org/10.1016/0022-1902\(79\)80457-1](https://doi.org/10.1016/0022-1902(79)80457-1).
- [37] L. Zhang, R.K. Brow, A Raman study of iron-phosphate crystalline compounds and glasses, *J. Am. Ceram. Soc.* 94 (2011) 3123–3130, <https://doi.org/10.1111/j.1551-2916.2011.04486.x>.
- [38] P. Wu, G. Eriksson, A.D. Pelton, Critical evaluation and optimization of the thermodynamic properties and phase diagrams of the CaO–FeO, CaO–MgO, CaO–MnO, FeO–MgO, FeO–MnO, and MgO–MnO systems, *J. Am. Ceram. Soc.* 76 (1993) 2065–2075, <https://doi.org/10.1111/j.1151-2916.1993.tb08334.x>.
- [39] M. Timucin, A. Morris, Phase equilibria and thermodynamic studies in the system CaO–FeO–Fe₂O₃–SiO₂, *Metallurgical Transactions* 1 (1970) 3193–3201, <https://doi.org/10.1007/BF03038437>.
- [40] L.C. De Jonghe, M.N. Rahaman, 4.1 sintering of ceramics, *Handbook of Advanced Ceramics: Materials, Applications, Processing and Properties*, 2 2003, p. 187, <https://doi.org/10.1016/B978-012654640-8/50006-7>.
- [41] Crespo Petit, F., Effect of Porosity on the Mechanical Properties of Zirconia Based Ceramics Obtained Via 3D Printing. *Universitat Politècnica de Catalunya*. (2016), <http://hdl.handle.net/2117/87702>.
- [42] T. Zhang, et al., Sintering, microstructure and grain growth of Fe-doped CeO₂. 9GdO₃ ceramics derived from oxalate coprecipitation, *J. Cryst. Growth* 274 (2005) 603–611, <https://doi.org/10.1016/j.jcrysgro.2004.10.011>.
- [43] Y. Xia, et al., Injectable calcium phosphate scaffold with iron oxide nanoparticles to enhance osteogenesis via dental pulp stem cells, *Artificial cells, nanomedicine, and biotechnology* (2018) 1–11, <https://doi.org/10.1080/21691401.2018.1428813>.
- [44] Y. Ikada, Challenges in tissue engineering, *J. R. Soc. Interface* 3 (2006) 589–601, <https://doi.org/10.1098/rsif.2006.0124>.
- [45] J. Zhang, et al., Good hydration and cell-biological performances of superparamagnetic calcium phosphate cement with concentration-dependent osteogenesis and angiogenesis induced by ferric iron, *J. Mater. Chem. B* 3 (2015) 8782–8795, <https://doi.org/10.1039/C5TB01440A>.
- [46] Q. Wang, et al., Response of MAPK pathway to iron oxide nanoparticles in vitro treatment promotes osteogenic differentiation of hBMSCs, *Biomaterials* 86 (2016) 11–20, <https://doi.org/10.1016/j.biomaterials.2016.02.004>.